

Improved strong lensing modelling of galaxy clusters using the Fundamental Plane: the case of Abell S1063.

G. Granata¹, A. Mercurio², C. Grillo^{1,3}, L. Tortorelli⁴, P. Bergamini⁵, M. Meneghetti^{5,6,7}, P. Rosati^{5,8},
G. B. Caminha⁹, and M. Nonino¹⁰

¹ Dipartimento di Fisica, Università degli Studi di Milano, Via Celoria 16, I-20133 Milano, Italy
e-mail: giovanni.granata@unimi.it

² INAF – Osservatorio Astronomico di Capodimonte, Via Moiariello 16, I-80131 Napoli, Italy

³ Dark Cosmology Centre, Niels Bohr Institute, University of Copenhagen, Jagtvej 128, DK-2200 Copenhagen, Denmark

⁴ Institute for Particle Physics and Astrophysics, ETH Zürich, Wolfgang-Pauli-Str. 27, CH-8093 Zürich, Switzerland

⁵ INAF – OAS, Osservatorio di Astrofisica e Scienza dello Spazio di Bologna, via Gobetti 93/3, I-40129 Bologna, Italy

⁶ National Institute for Nuclear Physics, viale Berti Pichat 6/2, I-40127 Bologna, Italy

⁷ Division of Physics, Mathematics, & Astronomy, California Institute of Technology, Pasadena, CA 91125, USA

⁸ Dipartimento di Fisica e Scienze della Terra, Università degli studi di Ferrara, via Saragat 1, I-44122 Ferrara, Italy

⁹ Max-Planck-Institut für Astrophysik, Karl-Schwarzschild-Str. 1, D-85748 Garching, Germany

¹⁰ INAF – Osservatorio Astronomico di Trieste, via G. B. Tiepolo 11, I-34131 Trieste, Italy

July 19, 2021

ABSTRACT

Aims. From accurate photometric and spectroscopic information, we build the Fundamental Plane (FP) relation for the early-type galaxies of the cluster Abell S1063. We use this relation to develop an improved strong lensing model of the cluster, and we decompose the cluster cumulative projected total mass profile into its stellar, hot gas and dark matter mass components. We compare our results with the predictions of cosmological simulations

Methods. We calibrate the FP using Hubble Frontier Fields photometry, and data from the Multi Unit Spectroscopic Explorer on the Very Large Telescope. The FP allows us to determine the velocity dispersions of all 222 cluster members included in the model from their measured structural parameters. As for their truncation radii, we test a proportionality relation with the observed half-light radii. Fixing the mass contribution of the hot gas component from X-ray data, the mass density distributions of the diffuse dark matter haloes are optimised by comparing the observed and model-predicted positions of 55 multiple images of 20 background sources, distributed over the redshift range 0.73 – 6.11. We determine the uncertainties on the model parameters with Monte Carlo Markov chains.

Results. We find that the most accurate predictions of the positions of the multiple images are obtained when the truncation radii of the member galaxies are approximately 2.3 times their effective radii. Compared to the previous work by Bergamini et al. (2019) on the same cluster, our model allows for the inclusion of some scatter on the relation between the total mass and the velocity dispersion of the cluster members. We notice a lower statistical uncertainty on the value of some model parameters. For instance, the main dark matter halo of the cluster has a core radius of 86 ± 2 kpc: the uncertainty on this value decreases by more than 30% with respect to the previous work. Taking advantage of a new estimate of the stellar mass of all cluster members from the HST multi-band data, we measure the cumulative two-dimensional mass profiles out to a radius of 350 kpc for all baryonic and dark matter components of the cluster. At the outermost radius of 350 kpc, we obtain a baryon fraction of 0.147 ± 0.002 . We study the stellar-to-total mass fraction of the high-mass cluster members in our model, finding good agreement with the observations of wide galaxy surveys, and some disagreement with the predictions of halo occupation distribution studies based on N -body simulations. Finally, we compare the features of the sub-haloes as described by our model with those predicted by high-resolution hydrodynamical simulations. We obtain compatible results in terms of stellar over total mass fraction. On the other hand, we report some discrepancies both in terms of maximum circular velocity, which is an indication of the halo compactness, and of sub-halo total mass function in the central cluster regions.

Key words. gravitational lensing: strong – galaxies: clusters: general – galaxies: clusters: individual (Abell S1063) – galaxies: kinematics and dynamics – dark matter – cosmology: observations

1. Introduction

The concordance, or Λ CDM, cosmological model, dominated by cold dark matter (CDM) and with a cosmological constant Λ , allows for specific predictions about the physical properties of dark matter (DM) haloes at different scales. CDM drives the hierarchical growth of structures in the Universe: the most massive DM haloes form from mergers of smaller objects and by accretion (e.g. Tormen 1997; Moore et al. 1999). Many of the less massive haloes are therefore found orbiting around the largest

structures: they are usually referred to as sub-haloes or substructures of a main halo. N -body cosmological simulations can be used to predict the number of sub-haloes around a halo of a given mass. They also show that DM haloes of any mass have a similar mass density profile, with a central cusp, usually described using the Navarro-Frenk-White (Navarro et al. 1996, 1997) or Einasto (Einasto 1965) profiles (e.g. Wang et al. 2020). Any significant discrepancy between these predictions and the observations may

imply that the formation of structures does not proceed as forecast by the Λ CDM model.

Galaxy clusters are especially well suited to test the predictions of cosmological simulations. Around 85 – 90% of their mass is made up of DM, between cluster-scale haloes and galaxy-scale haloes or sub-haloes. The remaining 10 – 15% is composed of baryons: hot X-ray emitting plasma and stars, which represent only $\approx 1\%$ of the total mass (Annunziatella et al. 2017; Sartoris et al. 2020). The entire baryonic mass budget of clusters can be measured from photometric and spectroscopic observations, in the near-IR, visible, and X-ray bands. Thus, if one determines the total mass distribution, one can disentangle that of the DM haloes and compare it with simulations (e.g. Die- mand & Moore 2011).

In the past few years, gravitational lensing has become one of the most effective techniques to study the total mass distribution of clusters (e.g. Natarajan & Kneib 1997), as it does not discriminate between baryons and DM. Strong lensing (SL) is especially effective in the central regions, or cores, of massive clusters (i.e., within ≈ 1 arcmin or ≈ 350 kpc, at $z = 0.5$), where the multiple images of background sources are found. In these regions, two important discrepancies between simulations and observations have emerged. First, several SL models suggest that the main DM haloes of clusters might have central flat cores (Sand et al. 2004), extended up to around 100 kpc (Grillo et al. 2015; Annunziatella et al. 2017; Bergamini et al. 2019, hereafter B19). This result seems to be confirmed on a homogenous and unbiased sample of massive lens galaxy clusters (Postman et al. 2012). A second discrepancy appears when comparing the amount and distribution of DM substructures (or sub-haloes). As found in Grillo et al. (2015), Munari et al. (2016) and Bonamigo et al. (2018), N -body simulations under-estimate the number of massive substructures near the cores of massive clusters. Furthermore, the number of predicted galaxy-scale SL events seems to imply that the mass distributions of these substructures are more concentrated than suggested by simulations (Meneghetti et al. 2020, hereafter M20).

Several Hubble Space Telescope (HST) programmes have recently been dedicated to the observation of SL phenomena caused by massive clusters. For instance, the Cluster Lensing And Supernova survey with Hubble (CLASH, Postman et al. 2012), the Hubble Frontier Fields (HFF, Lotz et al. 2017) campaign, and the Reionization Lensing Cluster Survey (RELICS, Coe et al. 2019) obtained multi-band HST images with an unprecedented depth for 25, 6, and 41 clusters, respectively. Moreover, spectroscopic campaigns such as CLASH-VLT (Dark Matter Mass Distributions of Hubble Treasury Clusters and the Foundations of Λ CDM Structure Formation Models, PI: P. Rosati, see Rosati et al. 2014), complemented with data from the new integral field spectrograph MUSE (Multi Unit Spectroscopic Explorer, Bacon et al. 2010), on the Very Large Telescope (VLT) have permitted secure identification of cluster members and precise redshift measurements for hundreds of multiply lensed sources. These data allowed for the construction of detailed SL models, whose accuracy can be assessed considering the distance between the observed positions of multiple images and those predicted by a model. The root mean square (rms) of this discrepancy can be as low as $0.3''$ (e.g. B19, Caminha et al. 2019), however still higher than the observational uncertainty on the position of the images, which can be less than a tenth of arcsecond. This might suggest that the total mass modelling of galaxy clusters needs to be further improved (see Meneghetti et al. 2017; Remolina González et al. 2018; Raney et al. 2020).

SL observations permit a very effective determination of the total mass enclosed within the multiple images of a single background source, but the same amount of mass can be obtained with relatively different mass distribution models (e.g. Limousin et al. 2016; Ghosh et al. 2021). This implies that the parameters that define a model often have a certain degree of degeneracy between them, which corresponds to a possible transfer of mass between the various components. Specifically, galaxy clusters are modelled with extended, cluster-scale mass clumps, to describe the main DM haloes (Natarajan & Kneib 1997) and the intra-cluster medium (ICM), and with smaller haloes, to represent the member galaxies (De Lucia et al. 2004). This last component is generally parametrised in SL models with spherical, truncated, isothermal profiles, defined only by their values of effective velocity dispersion and truncation radius, in order to reduce the number of optimised free parameters. Furthermore, their values are usually linked to the luminosity of each cluster member with two power-law scaling relations (e.g. Richard et al. 2014; Grillo et al. 2015; Monna et al. 2017). This approach is equivalent to using a Faber-Jackson scaling law (Faber & Jackson 1976) to determine the value of the velocity dispersion of an elliptical galaxy.

Information on the kinematics of galaxies can significantly reduce the degeneracy between the parameters of a SL model. Observations of galaxy-scale SL events by the Sloan Lens ACS (SLACS) survey allowed for a precise determination of the slope of the total mass density profile of massive lens galaxies (Koopmans et al. 2006). In recent years, velocity dispersion measurements have also become available for several members in some galaxy clusters. Monna et al. (2015) used spectrography from the Hectospec fiber spectrograph at the MMT and early CLASH data for 21 members of the cluster Abell 383, showing a significant reduction of the degeneracy between the SL model parameters. B19 refined and significantly extended this method to three CLASH clusters: MACS J1206.2–0847, MACS J0416.1–2403, and Abell S1063. The integral field data provided by MUSE permitted to obtain velocity dispersion measurements for 40–60 galaxies for each cluster. These data have been exploited to estimate the values of the slope and normalisation of the Faber-Jackson relation for those members. This has, in turn, been used as a prior to determine the exponent of the power-law relation which binds the total mass of sub-haloes to their luminosity. The new data and procedure have allowed for a more accurate mass assignment to the diffuse and sub-halo components, reducing the degeneracy between their parameters. This is crucial both to infer the DM mass density profile in the central regions of a cluster and to determine precisely its sub-halo mass function.

This technique has enabled a first step towards a more accurate mass modelling of the cluster members, but a single power-law relation between their total mass and luminosity may be inaccurate on the very large total mass range of member galaxies ($10^9 - 10^{13} M_{\odot}$). In order to improve on the adopted scaling relations for members, in this work we will consider the so-called Fundamental Plane (FP) relation (Dressler et al. 1987; Djorgovski & Davis 1987; Bender et al. 1992), which has a lower scatter than the Faber-Jackson law. We will focus on one of the three clusters considered by B19, namely Abell S1063 (AS1063). We choose it due to its rather regular morphology and because we have at our disposal line-of-sight velocity dispersion measurements for a sizable subset of cluster members (Mercurio et al., in prep.), for which we also have an estimate of their effective radius and magnitude. We can therefore use these galaxies to obtain the best-fit values of the parameters that define the FP.

The paper is organised as follows. In Sect. 2, we give details on our photometric and spectroscopic data and on how they were analysed and reduced for our objectives. In Sect. 3, we describe our strong lensing model built with the FP, while in Sect. 4 we present the analysis and discussion of the results of the optimisation, and the comparison with the previous model by B19. In Sect. 5, we show the cumulative, projected mass profiles for all the baryonic and DM components of our model. In Sect. 6, we compare our results with the predictions of stellar-to-halo mass relations derived from N -body simulations. In Sect. 7, we compare the stellar-to-total mass fraction and the compactness of the sub-haloes in our model with those suggested by recent high-resolution hydrodynamical simulations. Finally, in Sect. 8, we summarise our most important conclusions.

In this work, we use a flat Λ CDM cosmology with $\Omega_m = 0.3$ and $H_0 = 70 \text{ km s}^{-1} \text{ Mpc}^{-1}$, in which $1''$ corresponds to a scale of 4.92 kpc at $z = 0.348$, the redshift of AS1063. All magnitudes are expressed in the AB system.

2. Abell S1063: data and analysis

AS1063, first identified in Abell et al. (1989), is a massive galaxy cluster at redshift $z = 0.348$ (a virial mass value of $(2.17 \pm 0.06) \times 10^{15} M_\odot$ was estimated by Sartoris et al. 2020). Despite its regular shape, it appears to have recently undergone an off-axis merger, as inferred by Gómez et al. (2012) and Rahaman et al. (2021) from X-ray data. Its high mass and redshift make it a very effective gravitational lens, which allows us to use the observed position of 55 spectroscopically confirmed multiple images from 20 background sources, distributed over a wide range of redshifts ($z = 0.73 - 6.11$, see Caminha et al. 2016), to build a SL model.

The cluster is also a very bright X-ray source ($L_X \approx 2.5 \times 10^{45} \text{ erg s}^{-1}$ in the 0.1 – 2.4 keV band), due to the emission of the hot ($T \approx 12 \text{ keV}$) ICM (Rahaman et al. 2021): it was identified as RXJ2248.7–4431 in the ROSAT All-Sky Survey (De Grandi et al. 1999).

2.1. Photometric data

AS1063 has been included in the two main photometric campaigns by the Hubble Space Telescope which, in the last decade, targeted SL phenomena in galaxy clusters. Firstly, it was one of the 25 clusters included in CLASH. Both the ACS (Advanced Camera for Surveys) and the WFC3 (Wide Field Camera 3) instruments were used to observe the clusters with 16 different broadband filters, from the near-UV to the near-IR. An even deeper view on AS1063 was obtained thanks to the HFF programme, which was assigned 840 HST orbits to target a selected sample of only six clusters, in seven different bands (HST/ACS F435W, F606W, and F814W and HST/WFC3 F105W, F125W, F140W, and F160W). Following Tortorelli et al. (2018), we will use the HFF photometric data in the F814W band, which corresponds to a rest-frame R-band for the cluster redshift, as it allows for a good signal-to-noise ratio down to magnitudes of around 28 and it has a lower full width at half maximum (FWHM) of the point spread function (PSF) when compared to the near-IR bands.

In order to obtain the parameters of the FP and consequently derive the values of the velocity dispersions of the cluster members, we need robust measurements of their magnitudes and effective radii. We adopt the prescriptions developed in Tortorelli et al. (2018) and further enhanced in Tortorelli et al. (in prep.),

by analysing the 222 galaxies that we include in our model. The galaxy surface brightness profile fitting consists of iterative steps, where we consecutively increase the size of the fitted images. We start by measuring the photometric properties with SExtractor (Bertin & Arnouts 1996). These properties are used as initial guesses for the more accurate galaxy light profile analysis with GALFIT (Peng et al. 2010). We cut stamps around each galaxy, fitting its light profile and those of closest galaxies. Then, the best-fitting parameter values are used as starting points for the following iterations, where we simultaneously fit all galaxies falling in the nine regions we separate our image into. Finally, the parameters obtained in the previous step are used as a starting point for the final simultaneous light profile fitting of all galaxies in the whole image.

The surface brightness profiles of the galaxies are fitted with GALFIT using a single Sérsic light profiles with seven free parameters (the two centre coordinates, major-to-minor axis ratio, position angle, major-axis effective radius, Sérsic index, and magnitude). For every galaxy, GALFIT is provided with different combinations of PSFs, background value estimates, and noise images, as described in Tortorelli et al. (2018). This allows us to average out the contribution of systematic effects in the surface brightness fit.

The spectral energy distribution (SED) obtained from the multi-band HST photometry also permits us to infer the stellar mass of the member galaxies, using composite stellar population models. Further details will be provided in Mercurio et al. (in prep.), where the authors use the HST photometry plus the MUSE spectra to fit the SEDs of the members with a delayed exponential star formation history, solar metallicity, and a Salpeter (Salpeter 1955) stellar initial mass function (IMF). The presence of dust is taken into account following Calzetti et al. (2000).

However, MUSE data are only available for a fraction of our sample. For those galaxies we compare their stellar mass values obtained including information from spectra with those derived without. We notice only a small systematic offset between the two estimates, thus we choose to consider, for all the members, the stellar masses obtained by using only the photometric data, so as to have a uniform sample. From this comparison, we also fix a conservative error of 0.22 on the decimal logarithmic value of the stellar mass.

2.2. Spectroscopic data

AS1063 was also targeted by several spectroscopic observations. It was one of the thirteen clusters included in the CLASH-VLT survey, a VLT/VIMOS Large Programme. A total of 16 masks were used on a field of ≈ 25 arcmin across, allowing for the measurement of 3607 reliable redshifts, 1109 of which identify cluster members (Mercurio et al., in prep.).

The integral field spectrograph MUSE has complemented the VIMOS spectroscopy in cluster cores. AS1063 was observed with two different pointings, centred in the NE and SW regions of the cluster (Karman et al. 2015; Caminha et al. 2016; Karman et al. 2017), with an exposure time of 3.1 and 4.8 hours and a seeing of $1.1''$ and $0.9''$, respectively. MUSE provided a total of 175 additional reliable redshifts, 104 of which refer to cluster members. Following Caminha et al. (2016), we identify as spectroscopic cluster members those galaxies whose redshift falls in the range $0.336 - 0.362$, corresponding to a rest-frame velocity range of $\pm 3000 \text{ km s}^{-1}$. On the other hand, multi-band CLASH data permit to identify photometric members with the method presented in Grillo et al. (2015).

The MUSE data are also deep enough for the measurement of the line-of-sight stellar velocity dispersion of a considerable fraction of the cluster members (80 out of 222). As in B19, we use the pPXF software (penalized pixel-fitting) by Cappellari & Emsellem (2004) for the measurement, but instead of using a fixed circular aperture of $0.8''$ for all members, we choose a wider one, of $2''$, and weigh each pixel with its corresponding surface brightness value: this choice has been found to provide velocity dispersion values equivalent to the central ones. The aperture was reduced to $0.5''$ for a member whose velocity dispersion measurement was strongly influenced by the effects of the diffuse light of the BCG. pPXF estimates the line-of-sight-velocity-distribution (LOSVD) parameters by comparing the observed spectra with a set of stellar templates from the MILES library (Vazdekis et al. 2010) convolved with a LOSVD. The code minimises a χ^2 function between the measured spectrum and a model.

3. Building the strong lensing model

We build our SL model using that by B19 as a basis and taking advantage of the information provided by the FP relation for a more accurate determination of the total mass of the cluster members. We will then compare our model with that by B19 to understand how the new modelling choices on the mass of the sub-haloes influence the reconstruction of the diffuse mass component of the cluster.

As in B19, we start from the same 55 spectroscopically confirmed multiple images produced by 20 sources presented in Caminha et al. (2016), and we model the various lens mass components with dual pseudo-isothermal elliptical (dPIE) mass density profiles (Limousin et al. 2005; Elíasdóttir et al. 2007), which are the ellipsoidal generalisation of a truncated isothermal sphere with a central core. Likewise, we use the publicly available strong lensing code LensTool (Kneib et al. 1996; Jullo et al. 2007; Jullo & Kneib 2009) in order to find the best-fit values of the parameters of our model. The dPIE profile is defined by seven free parameters: two for the centre position, the ellipticity e and its position angle θ_e , the central velocity dispersion σ_0 , and the core and truncation radii r_c and r_t , respectively. The projected mass density of a spherical dPIE as a function of the two-dimensional distance from the centre R is (Elíasdóttir et al. 2007)

$$\Sigma(R) = \frac{\sigma_0^2}{2G} \frac{r_t}{r_t - r_c} \left(\frac{1}{\sqrt{r_c^2 + R^2}} - \frac{1}{\sqrt{r_t^2 + R^2}} \right). \quad (1)$$

LensTool actually parametrises the dPIE profile with a fiducial velocity dispersion which is related to the central velocity dispersion by $\sigma_{\text{LT}} = \sqrt{2/3}\sigma_0$ (see Elíasdóttir et al. 2007; Agnello et al. 2014, and Appendix C in B19). The diffuse, cluster-scale, DM haloes are represented with an elliptical dPIE, close to the brightest cluster galaxy (BCG) position, and a spherical dPIE with vanishing core radius, whose position is free to vary on an area of $150'' \times 120''$ centred in the NE region of the cluster. This second halo is necessary to reproduce some arcs in the NE region and its presence is compatible with the post-merger scenario of the cluster. As in B19, the hot gas mass component is completely fixed by the Chandra X-ray data, reduced in Bonamigo et al. (2018). This component is modelled with three dPIE mass profiles, whose parameters are not optimised. The position of each multiple image and source is identified by two coordinates. As the positions of the sources are not known, 55 multiple images

and 20 sources correspond to, respectively, 110 observables and 40 free parameters. The two cluster-scale DM clumps have nine further parameters: the values of the coordinates of the centre and of the velocity dispersions are free for both haloes, while those of the core radius, ellipticity and orientation angle are only optimised for the main halo. There is therefore a total of 49 free parameters, leading to 61 degrees of freedom.

As anticipated, the main difference with the model obtained in B19 is in the way we assign mass to the cluster members. They are modelled as spherical dPIE profiles with a negligible core radius, so that their total mass is entirely fixed by their values of velocity dispersion and truncation radius. To estimate the velocity dispersion of all member galaxies from their measured effective radius and surface brightness, we use the FP relation, since the vast majority of cluster members are early-type galaxies, as confirmed by our morphological analysis. As for the truncation radius of the members, we choose it as a multiple of their effective radius, as suggested by some previous studies (e.g. Mo et al. 1998). Kravtsov (2013) also found that the half light radius and the truncation radius are approximately proportional to each other, and that the ratio between them mostly depends on the angular momentum acquired from tidal torque by the halo during its formation. It has to be noted that the value of the ratio has been obtained by Kravtsov (2013) on a sample including early-type galaxies at much lower redshifts than our cluster. We test several values for this ratio, optimising all the free parameters describing the total mass distribution of the cluster each time, and finally choosing the ratio that allows for the lowest rms value between the observed and model-predicted positions of the multiple images.

3.1. The Fundamental Plane of Abell S1063

The FP is an empirical relation between the logarithm of the effective radius (i.e., the bi-dimensional radius inside which half of the total luminosity is emitted) R_e , the average surface brightness within it, SB_e , and the logarithm of the central stellar velocity dispersion σ_0 . The FP can be written as

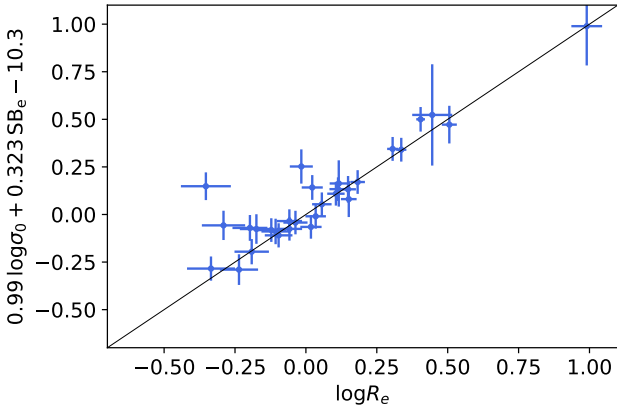
$$\log R_e = \alpha \log \sigma_0 + \beta \text{SB}_e + \gamma. \quad (2)$$

We consider R_e as measured in kpc, and σ_0 in km s^{-1} , whereas SB_e is defined as $(1 \text{ mag arcsec}^{-2}) \left(\frac{m}{1 \text{ mag}} + 2.5 \log \left(\frac{2\pi R_e^2}{1 \text{ kpc}^2} \right) \right)$, where m is the total magnitude measured using GALFIT.

As anticipated, MUSE observations and their subsequent analysis in Mercurio et al. (in prep.) provide us with line-of-sight central stellar velocity dispersions, σ_0 , for 80 out of the 222 member galaxies included in the model. As the FP is actually only valid for early-type galaxies, we need to ensure that the values of its parameters are not influenced by galaxies to which the FP relation does not strictly apply. There are different ways of selecting ETGs, based on their morphologies, colours, and stellar populations. In Tortorelli et al. (2018), it has been shown that ETGs selected via a Sérsic index value $n > 2.5$, elliptical morphology and a passive stellar population constitute a coeval population. Therefore, we select ETGs for which the FP applies as those galaxies with Sérsic index $n > 2.5$. Furthermore, we abide by the criteria introduced in B19, based on the robustness of the velocity dispersion measurements by pPXF on simulated spectra, thus including only those with a spectrum signal-to-noise ratio greater than 10 and $\sigma_0 > 80 \text{ km s}^{-1}$. We also exclude two further galaxies: one of them is in the diffuse light of the BCG, while the second is very close to another member which influences the velocity dispersion measurement. This leaves us with a total of

Table 1. Best-fit values and 1σ errors of the parameters of the FP.

Parameter	Value
α	0.99 ± 0.17
β	0.323 ± 0.029
γ	-10.3 ± 1.0

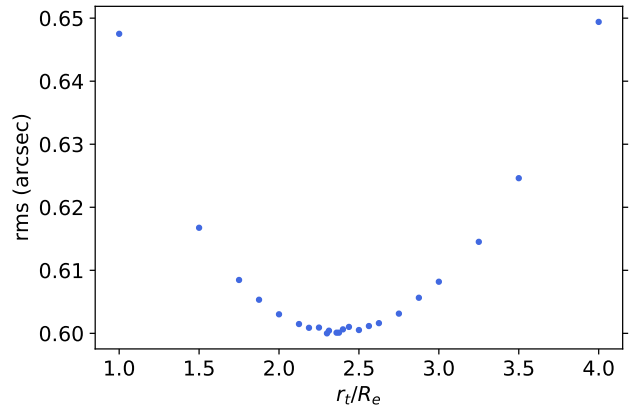

Fig. 1. Distribution around the FP of the 30 members selected to determine its parameters, with the 1σ uncertainties obtained through the error propagation. For the physical quantities, we use the units listed in the main text.

30 spectroscopically confirmed cluster members, out of the 80 for which we had a measurement of the stellar velocity dispersion, that we use as a basis to estimate the parameters of the FP relation.

To obtain the FP parameter values, we perform an optimisation using the code `ltsfit`, developed by Cappellari et al. (2013) for robust fits of lines or planes. A linear regression algorithm is used on the data to derive a first value for the parameters. A σ dispersion around the plane is defined as the range in which 68% of the values fall. The points that lie at more than 3σ from the plane determined by the first regression are clipped and the code repeats the procedure iteratively with the remaining points, until no new member is discarded and the final parameter values are obtained. As for the errors on the observables, we use the propagated experimental uncertainty. Tortorelli et al. (2018) find, for the same cluster, an average uncertainty of 0.09 kpc on R_e and of $0.19 \text{ mag arcsec}^{-2}$ on SB_e for galaxies with $m_{F814W} \leq 22.5$, which are significantly higher than what we obtain through the error propagation for several members. We choose 0.09 kpc and $0.19 \text{ mag arcsec}^{-2}$ as lower limits for those uncertainties. We list the best-fit values of α , β , and γ obtained with `ltsfit` in Table 1.

The values of α and β , which do not depend on redshift, are compatible with those reported in the literature (e.g. Barr et al. 2006).

As clear from Figure 1, there are just very few outliers around the FP: their photometric and spectroscopic analyses have been checked and confirmed. They do not however influence the values of the FP parameters, as they are clipped during the optimisation procedure. To evaluate the accuracy of the calibrated FP at predicting cluster member central velocity dispersions, we can compare the measured values of σ_0 with those obtained through the relation for the 30 members used to derive the parameters. We call these values $\sigma_{0,FP}$. The median value of


Fig. 2. Values of the rms difference between the observed and model-predicted positions of the 55 multiple images used in our model as a function of the ratio between the truncation and effective radii of the cluster members.

the ratio $\frac{\sigma_{0,FP}}{\sigma_0}$ is 0.98, with a standard deviation of 0.20, corresponding to a $\chi^2_{\text{red}} = \frac{\sum_{i=1}^{30} (\sigma_{0,FP} - \sigma_0)^2}{30\sigma_0^2} = 0.05$, denoting a low scatter around the plane, as shown by Figure 1.

3.2. The best-fit model

From the best-fit FP parameters, we can compute the value of the central stellar velocity dispersion for all members. As anticipated, we take the value of the truncation radius of the members as a multiple of their measured effective radius, testing several proportionality constant values and re-optimising the values of all the parameters describing the diffuse DM components each time.

To determine the values of the parameters of the best-fit model, we use the χ^2 minimisation implemented in `Lenstool`. The χ^2 function is defined as

$$\chi^2(\theta) = \sum_{j=1}^{N_{\text{fam}}} \sum_{i=1}^{N_{\text{img}}^j} \left(\frac{\|\mathbf{x}_{\text{obs},i,j} - \mathbf{x}_{\text{pred},i,j}(\theta)\|^2}{\sigma_{x,i,j}} \right), \quad (3)$$

where N_{fam} is the number of multiple image families considered to evaluate the precision of our model and N_{img}^j is the number of multiple images that compose the j -th family. $\mathbf{x}_{\text{obs},i,j}$ and $\sigma_{x,i,j}$ are, respectively, the observed position of the i -th image of the j -th family and its uncertainty. Finally, $\mathbf{x}_{\text{pred},i,j}(\theta)$ is the position of the same image as predicted by the model defined by the set of parameter values θ . As in Bonamigo et al. (2018) and B19, we assume an error of $0.5''$ on the HST multiple images and of $1''$ for the multiple images only found in the MUSE data.

We find that the lowest values of the χ^2 are obtained when the proportionality constant varies between 2.2 and 2.5, as clear from Figure 2. In particular, we obtain the absolute lowest value of χ^2 for $r_t = 2.3R_e$. This value is at least an order of magnitude smaller than that suggested by halo abundance matching studies (Kravtsov 2013). In this case, we find that the minimum χ^2 has a value of 84.92, with 61 degrees of freedom, which corresponds to a rms value of $0.60''$.

In Table 2, the best-fit values of the free parameters of this model and of that by B19 are listed. The positions of the clumps are referred to the centre of the BCG. The ellipticity of the main halo is defined as $e = \frac{a^2 - b^2}{a^2 + b^2}$, where a and b are the

Table 2. Best-fit values and 1σ errors of the parameters of our SL model, compared with those obtained in B19. The index 1 refers to the main, central halo, the index 2 to the secondary, spherical one.

Parameter	This work	B19
x_1 (")	$1.21^{+0.24}_{-0.24}$	$1.40^{+0.23}_{-0.23}$
y_1 (")	$-0.69^{+0.19}_{-0.19}$	$-0.74^{+0.16}_{-0.17}$
e	$-0.63^{+0.01}_{-0.01}$	$-0.63^{+0.01}_{-0.01}$
θ_e (°)	$-38.79^{+0.25}_{-0.26}$	$-38.75^{+0.22}_{-0.23}$
r_c (")	$17.37^{+0.35}_{-0.37}$	$18.06^{+0.53}_{-0.52}$
$\sigma_{\text{LT},1}$ (km s $^{-1}$)	$1159.1^{+6.8}_{-7.4}$	$1162.4^{+6.4}_{-6.7}$
x_2 (")	$-50.4^{+4.5}_{-5.6}$	$-50.2^{+3.7}_{-4.4}$
y_2 (")	$27.5^{+3.2}_{-2.7}$	$26.8^{+2.4}_{-2.2}$
$\sigma_{\text{LT},2}$ (km s $^{-1}$)	214^{+29}_{-26}	221^{+24}_{-22}

major and minor semi-axes. The orientation angle is measured counter-clockwise from the positive x axis. For both models, we determine the statistical uncertainties on the parameters using the Monte Carlo Markov chains as implemented by LensTool, based on the BayeSys algorithm (Jullo et al. 2007). To obtain a reliable estimate of the uncertainties on the parameter values from the MCMC sampling, the observational uncertainty on the positions of the multiple images is increased to get a χ^2 value close to the number of degrees of freedom.

4. Comparison and discussion

In this section, we compare our model with that presented in B19, which is our starting point and reference. Using the same code, LensTool, B19 obtain a minimum value of χ^2 of 69.90, which corresponds to a value of the rms on the positions of the 55 multiple images of $0.55''$, slightly lower than our value of $0.60''$. This small increase in the rms value with respect to B19 was expected, as in our model the mass component representing the member galaxies has less freedom. In B19, the truncation radius and the fiducial velocity dispersion of the i -th member are obtained through power laws from its luminosity L_i , specifically

$$\begin{aligned} \sigma_{\text{LT},i} &= \sigma_{\text{LT}}^{\text{ref}} \left(\frac{L_i}{L_0} \right)^{0.27}, \\ r_{t,i} &= r_t^{\text{ref}} \left(\frac{L_i}{L_0} \right)^{0.66}, \end{aligned} \quad (4)$$

where L_0 is the luminosity of the BCG. The reference values in the relations ($\sigma_{\text{LT}}^{\text{ref}}$ and r_t^{ref}) are free to vary, increasing the number of free parameters from 49 to 51. This additional freedom corresponds to some extent to a possible mass exchange between the member galaxies and the diffuse cluster-scale DM haloes. In our model, the total mass component of the cluster galaxies is completely fixed by the observations through the FP, and only the two main DM haloes have their mass free to vary.

We first focus on how mass is assigned to the member galaxies. For both models, cluster members are modelled as dPIEs with vanishing core radius and zero ellipticity, so their total mass can be obtained as

$$M = \frac{\pi \sigma_0^2 r_t}{G} \quad (5)$$

Table 3. rms and maximum likelihood \mathcal{L} values for our model and for the one presented in B19. The maximum value of the likelihood is provided by LensTool.

Parameter	This work	B19
Observables	110	110
Free parameters	49	51
$\ln \mathcal{L}$	-65.94	-58.43
rms	$0.60''$	$0.55''$

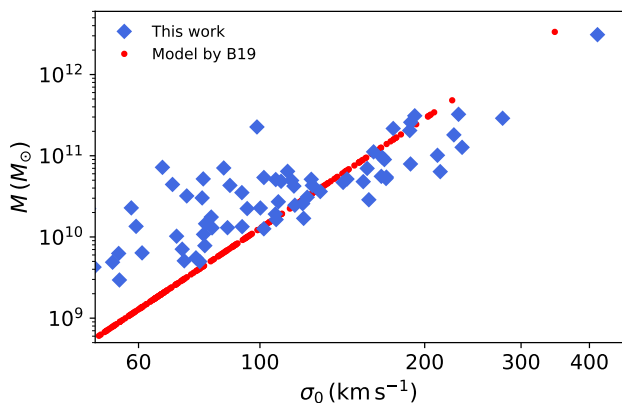


Fig. 3. Total mass of the cluster members as a function of their velocity dispersion. In blue: values predicted by our model. In red: values predicted by the model presented in B19.

In B19, r_t and σ_0 are derived, for each member, with the two power law scaling relations reported in Eq. 4, which imply that $M \propto \sigma_0^{4.44}$. Such a precise and simple relation between M and σ_0 , with no scatter, might be an oversimplification, given the large range in total mass value and the great variety in galactic morphology. The use of two measured observables and a more accurate relation (the FP) should allow for a more complex and realistic dependence of M from the other observables. This is shown in Figure 3: the $M(\sigma_0)$ relation has a visible scatter, which the model by B19 could not include. The relation also shows a shallower slope (a bi-logarithmic fit on the members with $\sigma_{0,\text{FP}} > 80 \text{ km s}^{-1}$ gives a slope value of around 2.4). The two models are similar in the high-mass regime and agree on the prediction of the total mass of the BCG. Despite being fixed by the FP with the same procedure as for all other cluster members, our model predicts a BCG total mass value of $3.10 \times 10^{12} M_\odot$, very close to that found in B19 ($3.35 \times 10^{12} M_\odot$), where it is *de facto* a free parameter.

As explained in Sect. 2, we measure the stellar mass values of all 222 member galaxies (Mercurio et al., in prep.) from HST multi-band photometric data, using a Salpeter IMF. By combining this with the results of Eq. 5, we can estimate the stellar fraction of the cluster members, computed as the ratio between their stellar mass and total mass values. As lensing models are more sensitive to the effects of high-mass members, we will focus only on the 50 galaxies with $\sigma_{0,\text{FP}} > 80 \text{ km s}^{-1}$. For this subset of members, the median value of the stellar fraction is 0.48, with a standard deviation of 0.26. From the model presented in B19, using the same stellar mass values, we obtain a smaller, but compatible median value of 0.25. Therefore our model predicts, on average, higher values for the stellar fraction, as illustrated in Figure 4.

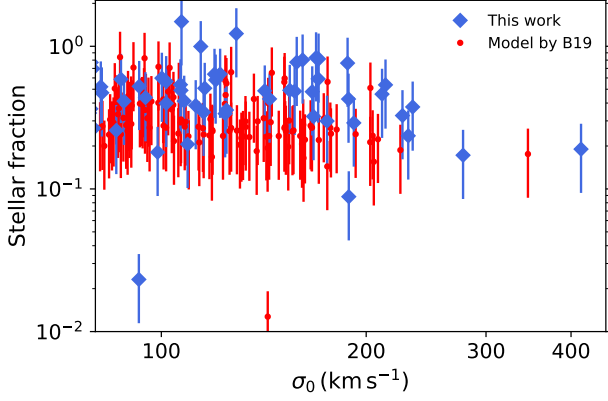


Fig. 4. Stellar fraction of the cluster members as a function of their central velocity dispersion for the 50 galaxies with $\sigma_{0,FP} > 80 \text{ km s}^{-1}$: comparison between the values obtained with our model (in blue) and those from the model in B19 (in red).

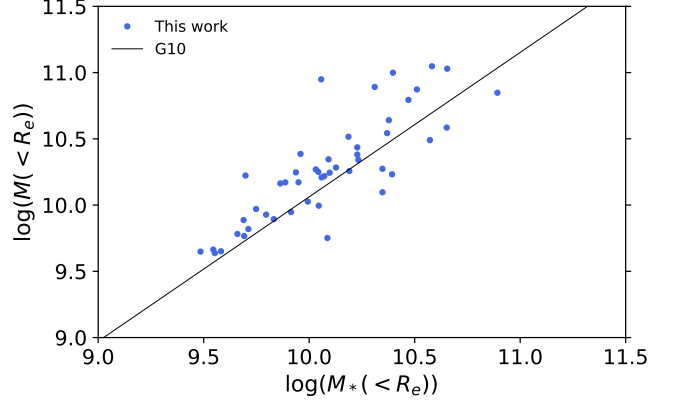


Fig. 5. Logarithmic values of the total mass as a function of the logarithmic values of the stellar mass, both projected within the effective radius, of all members with $\sigma_{0,FP} > 80 \text{ km s}^{-1}$. The plot also shows the relation found by Grillo (2010).

We now compare our stellar fraction values with those of other massive early-type galaxies. Grillo (2010) studies the projected dark matter fraction within the effective radius for a sample of nearly 1.7×10^5 early-type galaxies from the Sloan Digital Sky Survey (SDSS) Data Release Seven (DR7), selected to reproduce well the physical properties of the lenses in the Sloan Lens ACS Survey (SLACS, Koopmans et al. 2009). He considered the values of the galaxy stellar mass as reported in the MPA/JHU catalogue, and obtained the values of the galaxy projected total mass within the effective radius, by assuming a one-component isothermal model, parametrised by the value of the measured central stellar velocity dispersion. He found that the best-fit linear relation between the logarithm of the projected total and stellar mass values within the effective radius, $M(< R_e)$ and $M_*(< R_e)$, respectively, is

$$\log(M(< R_e)) = -0.58 + 1.09 \log(M_*(< R_e)), \quad (6)$$

As far as the cluster members of AS1063 are concerned, assuming that light traces stellar mass, $M_*(< R_e)$ is half of their total stellar mass, as R_e is defined as the two-dimensional radius within which half of the total light is emitted. The stellar mass values of our cluster members have been obtained assuming a Salpeter stellar IMF, while those presented by Grillo (2010) are derived adopting a Chabrier stellar IMF (Chabrier 2003). To compare the two samples, we use a constant conversion factor (0.585, from Speagle et al. 2014) between the stellar mass values obtained with a Salpeter and a Chabrier stellar IMF. As for the projected total mass, the mass of a dPIE profile with a vanishing core radius enclosed within a two-dimensional radius R is (Elíasdóttir et al. 2007)

$$M(< R) = \frac{\pi \sigma_0^2}{G} \left(R - \sqrt{r_t^2 + R^2} + r_t \right). \quad (7)$$

For $r_t = 2.3R_e$, Eqs. 7 and 5 give $M(R_e) \approx 0.344M$, where M is the total mass. As Figure 5 shows, we find that our members follow well the relation found by Grillo (2010), with a scatter around it that increases with the value of the stellar mass. This is significant, as we are considering in both cases massive elliptical galaxies, but the values of their stellar fractions are obtained with different methods. The observed agreement suggests that the inner (i.e., within R_e) mass structure of the massive cluster

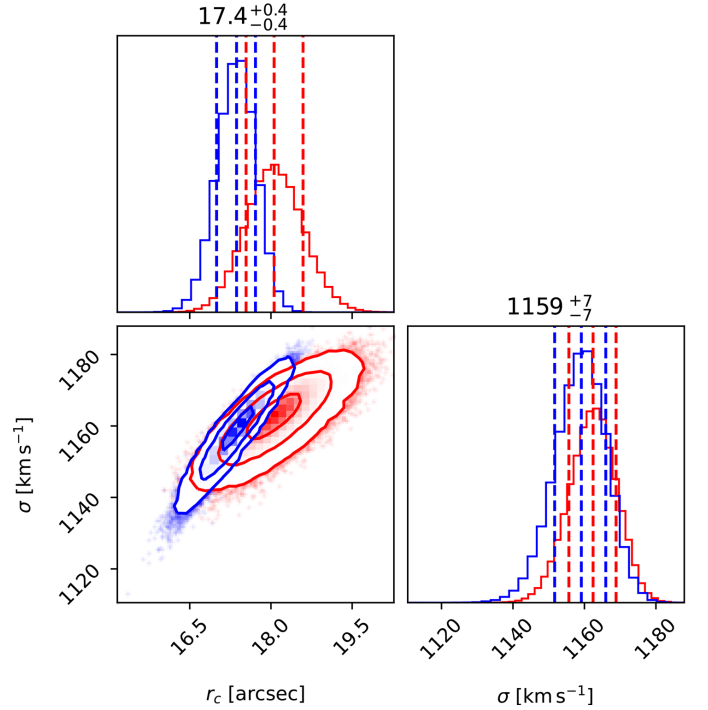


Fig. 6. Posterior probability distributions of r_c and σ_{LT} of the main DM halo and degeneracy between them for our model (in blue) and that by B19 (in red). The 16th, 50th and 84th percentiles of the marginalized probability distributions are marked with dashed vertical lines for both models. The values of these percentiles for our model are reported above the histograms.

members of AS1063 and of massive early-type galaxies living in different environments might be very similar. Note that the relation shown in Figure 5 has been adapted from Eq. 7 for the case of stellar mass values determined using a Salpeter IMF.

Looking instead at the diffuse components of the two models, from the Monte Carlo sampling of the marginalised posterior probability we see a drop of more than 30% of the uncertainty on the value of the core radius of the main DM halo (see Figure 6). The scatter between the core radius and the velocity dispersion is also considerably reduced. This indicates that a more accurate estimate of the total mass of the member galaxies has resulted

Table 4. Projected mass within a two dimensional radius $R = 350$ kpc of the baryonic components.

Component	$M(10^{12} M_{\odot})$
Stars	2.4 ± 0.6
ICM	63.3 ± 0.6

in distributions of the parameters with a lower statistical uncertainty.

Monte Carlo chains also show that the core of the main diffuse DM halo has a radius of 86 ± 2 kpc. Our result is in line with those from SL models of similar galaxy clusters (e.g. B19, Grillo et al. 2015; Annunziatella et al. 2017; Lagattuta et al. 2017; Caminha et al. 2019; Diego et al. 2020), which found that cluster haloes are very well described by cored isothermal mass density profiles.

5. Mass profile decomposition

In this section, we will obtain and present the cumulative projected mass profiles of all the cluster mass components: the stellar mass and the DM of cluster members, the ICM, and the diffuse, cluster-scale DM. We will only consider the mass distribution out to a projected radius R of 350 kpc from the centre of the BCG, to avoid including regions not covered by our photometric data, where the cluster member catalogue is incomplete.

5.1. The baryonic mass components

To measure the stellar mass profile of the cluster, we start from the surface brightness best-fit model of each cluster member in the HST F814W band, shown in Figure 7, which we already used to derive their structural parameters. Figure 7 shows that our procedure does not allow to completely account for the intra-cluster light (ICL) distribution, which also contributes to the cluster stellar mass budget. However, the ICL in AS1063, especially far from its BCG, is less important than in other clusters of comparable mass. Similarly to Annunziatella et al. (2017), we estimate an average value for the stellar mass-to-light ratio (M_*/L) of all cluster members from their total luminosity and total stellar mass. The choice of considering a constant ratio is an approximation, as the value may change in the different regions of each galaxy, as well as among galaxies. However, several galaxies are included in each radial bin above 50 kpc, and this should reduce the impact of this approximation. We then use this ratio to convert the cumulative luminosity profile into a cumulative stellar mass profile. As above, we consider an error of 0.22 on $\log(M_*)$ of each galaxy, and we apply the same uncertainty on the total value in each radial bin of the projected profile.

We take the cumulative projected ICM mass profile from Bonamigo et al. (2018): following their result, we impose a relative error of approximately 1% on each bin. The total projected mass of the three haloes used to model the hot gas, within a bi-dimensional radius of 350 kpc, is reported in Table 4.

5.2. The dark matter mass distribution

In Sect. 3, we described our modelisation of the DM mass distribution: an ellipsoidal, pseudo-isothermal, non-truncated clump, and a less massive, spherical one represent the cluster-scale DM haloes. On the other hand, 222 spherical, truncated, isothermal

Table 5. Comparison between the projected mass within a two-dimensional radius $R = 350$ kpc for the DM components in our model and in that by B19. The errors are, in both cases, estimated from 100 random models extracted from the MCMC chains, and the 14th and 68th percentiles are shown.

Component	Our model $M(10^{12} M_{\odot})$	Model from B19 $M(10^{12} M_{\odot})$
Diffuse DM	377 ± 2	377 ± 2
DM sub-haloes	4.4 ± 0.6	6.9 ± 0.9
Total	447 ± 2	449 ± 2

haloes are introduced to describe the total mass of cluster members. To disentangle the mass distribution of DM sub-haloes, we therefore need to subtract the stellar mass profile to it.

The parameter space sampling obtained with the Monte Carlo method can be used to estimate the error on the DM cumulative mass profiles. We extract 100 random sets of parameter values from the chains and derive the cumulative mass profiles of each corresponding model. In Figure 8, the error bars show the 16th and 84th percentiles of the mass profiles associated to all the models extracted from the chains. We perform this analysis for our model and repeat it for the model by B19. In the first case, the total mass of the cluster members is fixed, so the uncertainty on the DM sub-halo mass profile is only associated to the error on the stellar mass. In the second case, instead, the mass of the cluster members is also optimised: MCMC chains provide us with an uncertainty on their mass, which is combined with that on M_* to obtain the error on the DM sub-halo cumulative mass profile.

We notice that the total mass of the cluster and the mass of the diffuse DM component are very well constrained by SL: the two models find very similar values and their statistical uncertainties are of approximately 1%. As a matter of fact, the two profiles are almost completely superimposed in Figure 8, and the error bars are very small. The mass of the DM sub-haloes, instead, slightly differs between the two models, especially in the outer regions, where our model predicts a lower value. A reason for this discrepancy might be in the different scaling laws that determine r_t in the two models. Comparing our results with the total mass profiles obtained, for the same cluster, with a full dynamical reconstruction (Sartoris et al. 2020), and with the X-ray hydrostatic method (Umetsu et al. 2016), we find very good agreement in the radial range considered. These two profiles are shown in Figure 7 by Sartoris et al. (2020).

The profiles measured from our model also allow us to obtain the two-dimensional, cumulative, stellar-, gas-, and baryonic-to-total mass fractions as a function of R , out to 350 kpc. In Figure 8, we report the results and compare the baryonic fraction profile with the cosmological baryon fraction value reported in the Planck 2018 results: 0.156 ± 0.002 , obtained from the ratio between $\Omega_b h^2$ and $\Omega_m h^2$, with information from the CMB (Cosmic Microwave Background) power spectrum and lensing reconstruction (see Planck Collaboration Planck Collaboration et al. 2020). The error bars of the profiles result from the propagation of the uncertainty on the cumulative values of the mass components. The fraction obtained at $R = 350$ kpc is 0.147 ± 0.002 . This value is similar to the cosmological value and consistent with what Bonamigo et al. (2018) reported for the same cluster at a comparable radius.

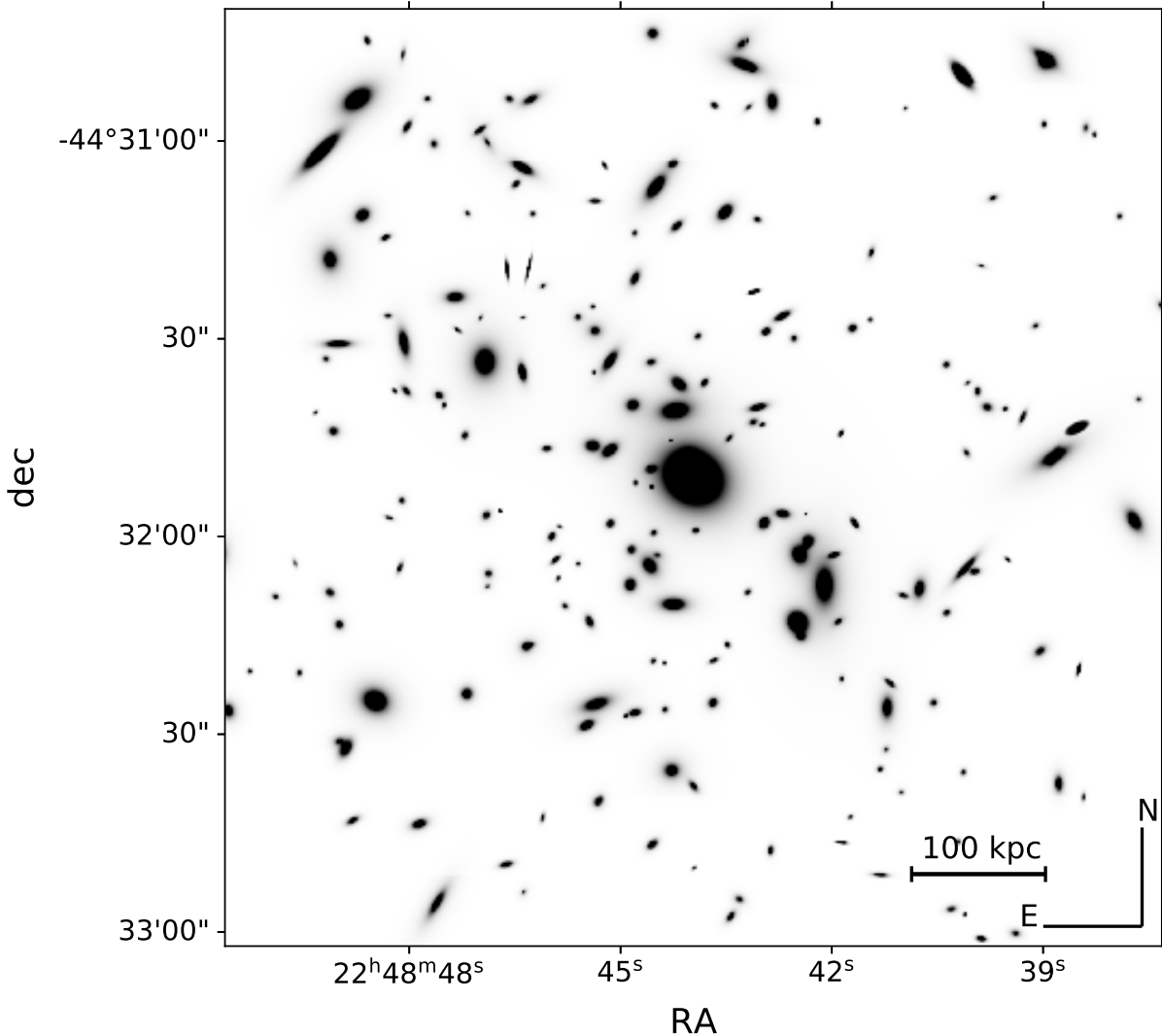


Fig. 7. Reconstructed surface brightness distribution of all cluster members used in the strong lensing model in HST F814W band. The field of view is 700 kpc wide and centred on the BCG to cover the entire region where the cumulative mass profile is obtained.

6. Comparison with halo occupation distribution studies

In this section, we compare the values of total the mass predicted for cluster members by our model with those obtained from the measured stellar mass values using halo occupation distribution (HOD) studies, based on cosmological N -body simulations. In the previous section, we have found that both our model and that by B19 lead to median values of the stellar-to-total mass ratio of massive member galaxies in the range between 0.25 and 0.5. As we will see, this result differs significantly from the predictions of statistical (sub)-halo abundance matching studies. We compare our results with the recent stellar-to-halo mass relation (SHMR) presented in Girelli et al. (2020). They consider the halo mass function derived from the cosmological N -body collisionless Λ CDM DUSTGRAIN-*pathfinder* simulation (Giocoli et al.

2018), which is complete for halo masses $M_h > 10^{12.5} M_\odot$, and extend it to lower masses. The simulation is built from a sample that also includes some cluster members, especially in the high-mass range. Then, taking the observed galaxy stellar mass of the COSMOS field (Scoville et al. 2007), they perform an abundance matching via a deterministic relation between halo and stellar mass. The SHMR is found by Girelli et al. (2020) to be in good agreement both with the observed clustering of massive galaxies and with the SHMR of clusters selected from spectroscopic data from the SDSS. The inclusion of some scatter on the value of the stellar mass leads to consistent results for the relation, so we will not consider it in the following analysis.

The obtained SHMR is valid from stellar mass values between $M_* \sim 10^8 M_\odot$ and $M_* \sim 10^{12} M_\odot$, from $z = 0$ to $z = 4$. The relation, using the parametrisation proposed by Moster et al.

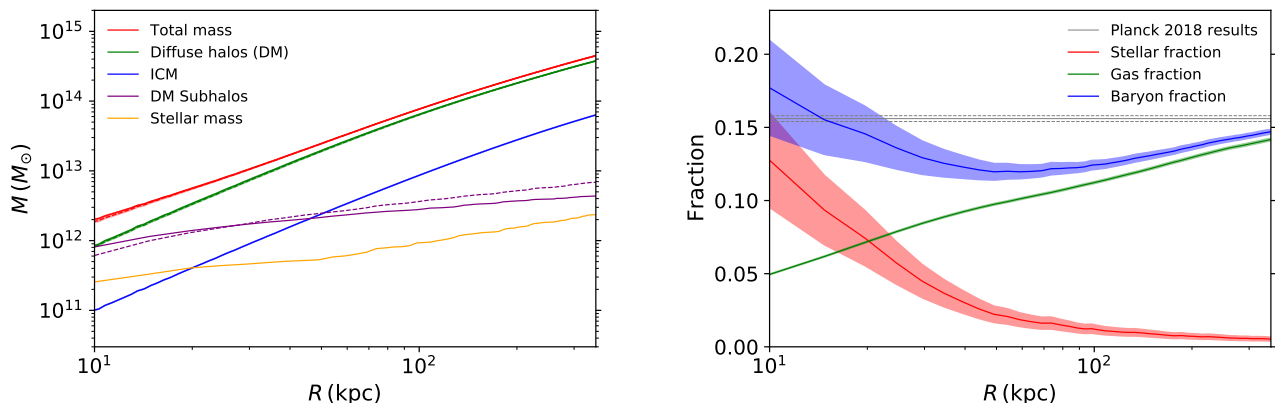


Fig. 8. Left panel: cumulative two-dimensional mass profiles for all baryonic and dark components of AS1063. The total mass profile and those of the diffuse DM haloes and of DM sub-haloes obtained from the model in B19, which differ from ours, are represented with dashed lines. Right panel: cumulative stellar-, gas- and baryonic-to-total mass fractions from our model. The value of the cosmological baryon fraction from the Planck Collaboration et al. (2020) is also shown.

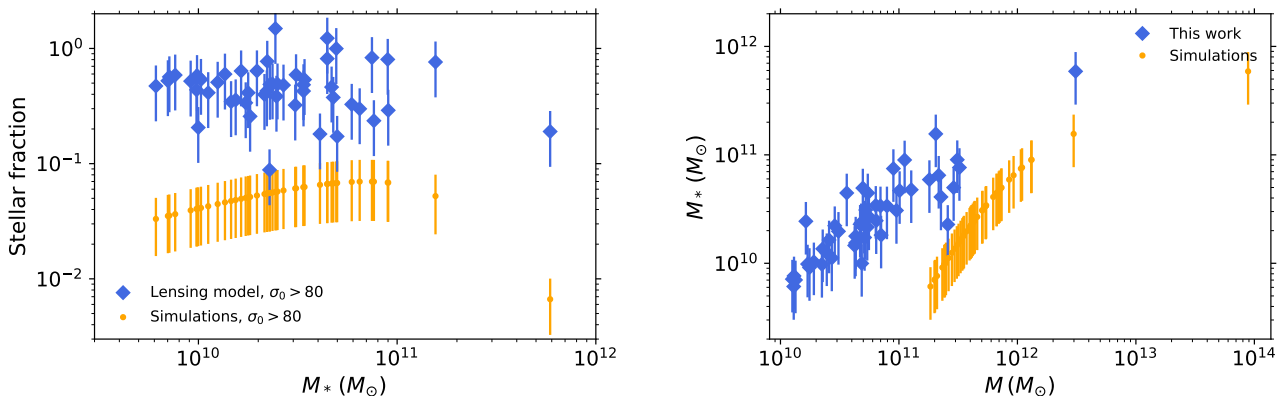


Fig. 9. Comparison between the values of the stellar over total mass fraction of the cluster members obtained with our lensing model (in blue) and with the SHMR (in orange). Only the 50 cluster members with $\sigma_{0,FP} > 80$ km s⁻¹ are shown. Left panel: stellar over total mass fraction of members as a function of their stellar mass. Right panel: stellar-to-halo mass relation.

(2010), can be written as

$$\frac{M_*(z)}{M_h} = 2A(z) \left[\left(\frac{M_h}{M_A(z)} \right)^{-\beta(z)} + \left(\frac{M_h}{M_A(z)} \right)^{\gamma(z)} \right]^{-1}, \quad (8)$$

where $A(z)$ is a normalisation factor, $M_A(z)$ a characteristic halo mass, and $\beta(z)$ and $\gamma(z)$ are the slopes of the relation in the low- and high-mass ranges, respectively. We adopt the values of the parameters found by Girelli et al. (2020) at the cluster redshift. We can then proceed by using Eq. 8 to compute the total halo mass of the members and, in turn, the values of their truncation radius from Eq. 5. We will finally compare these values of the truncation radii with those we obtained in our model, from the effective radii of the members. We do not consider any uncertainty on the parameter and stellar mass values, as we will show that the differences are large and cannot be reconciled by the statistical errors. We notice that the SHMR presented by Girelli et al. (2020) was derived adopting a Chabrier stellar IMF. To make use of the relation to estimate the halo mass of the cluster members from their stellar mass, we adopt the same conversion factor of 0.58 between the Salpeter and Chabrier IMFs that we previously used.

Using the SHMR, the projected mass of the DM sub-haloes within a bidimensional radius of 350 kpc grows to $6.1_{-0.1}^{+0.1} \times$

$10^{13} M_\odot$, larger by a factor of almost 14. The ratio $r = \frac{M_{SHMR}}{M_{model}}$, where M_{SHMR} is the total mass obtained for a member from SHMR, and M_{model} is the corresponding total mass as in the SL model, has a median value of 8.7 for the members with $\sigma_{0,FP} > 80$ km s⁻¹. For these selected high-mass members, as shown in Figure 9, the median value of the stellar fraction decreases from 0.48 (with a standard deviation of 0.26) to 0.055 (with a standard deviation of 0.014). The value of r is also that of the ratio between the value of the truncation radius of a sub-halo obtained from simulations and that adopted in our model.

We perform a new run of the model, fixing the total mass of each cluster member to the value obtained from the SHMR. Optimising the free parameters of the two diffuse DM haloes, the value of the rms between the observed and predicted positions of the 55 multiple images grows by more than 25% (to 0.76''), despite having the same number of degrees of freedom. The results of the optimisation suggest that the values of the total mass of the cluster members, and therefore, fixing σ_0 , of their truncation radius, is probably overestimated by the SHMR.

An important reason for this discrepancy may be the fact that the Λ CDM DUSTGRAIN-*pathfinder* simulation only includes collisionless particles. Thus, it does not consider the effects of the interplay between DM and baryons, which are very

important during galaxy formation. For instance, [Smith et al. \(2016\)](#) found that DM stripping happens earlier than star stripping, which could at least partially justify the differences in the stellar fraction.

7. Comparison with cosmological hydrodynamical simulations

In this section, we contrast the features of the sub-haloes in our new SL model with the predictions of the most recent cosmological hydrodynamical simulations. In the first sub-section, we consider the stellar over total mass fraction of sub-haloes. In the second sub-section, we study the relation between their maximum circular velocity and total mass, which is an indication of their compactness ([Munari et al. 2016](#)).

7.1. Stellar fraction of cluster members

As reported in Section 4, our model predicts a median stellar-to-total mass fraction value of 0.48, with a standard deviation of 0.26, for the 50 cluster members with $\sigma_{0,FP} > 80 \text{ km s}^{-1}$. We have seen, in Section 6, that a SHMR obtained with a HOD procedure on the results of N -body cosmological simulations underestimates this value with respect to our model by almost an order of magnitude. We will now repeat the comparison with high-resolution cosmological hydrodynamical simulations ([Planelles et al. 2014](#); [Rasia et al. 2015](#)), carried out with the GADGET-3 code ([Springel 2005](#)). To perform a comparison between the features of sub-haloes as predicted by the simulation and by our model, we consider 18 simulated clusters with $M > 10^{15} M_{\odot}$ at redshift $z = 0.38$ and perform three spatial projections of their mass distributions. We then extract their substructures from the SUBFIND algorithm ([Springel et al. 2001](#); [Dolag et al. 2009](#)) catalogue¹. We impose a minimum value of the velocity dispersion of 80 km s^{-1} , as in the previous analyses carried out in this paper, and a maximum projected distance from the cluster centre of $R = 0.15 r_{vir}$, where r_{vir} is the cluster virial radius. We thus obtain a catalogue of 1756 substructures, and we compute the stellar mass fraction for each of them. Again, as the simulations considered use a Chabrier IMF to obtain the stellar mass of substructures, we use the previously presented conversion factor to compare them with our measured stellar mass values, for which [Mercurio et al.](#) (in prep.) used a Salpeter IMF. We obtain a median stellar mass fraction value of 0.37, with a standard deviation of 0.18, in good agreement with the value suggested by the lensing model. Figure 10 also shows that the simulated sample has a similar relation between the stellar mass fraction and the total subhalo mass with respect to our model. We note that the subhaloes extracted from the simulated catalogue have a slightly higher (around $3 \times 10^{10} M_{\odot}$) lower limit for the total mass compared to those extracted from the SL model adopting the same criterion. This seems to suggest that at a fixed velocity dispersion simulated substructures have, on average, a higher total mass. In the next sub-section, we will address this issue in light of the recent studies that have focussed on it.

7.2. Compactness of the cluster's sub-haloes

Significant differences between the sub-halo compactness obtained from lensing models and cosmological simulations have recently been reported by M20. They considered 11 SL models

¹ The simulation snapshots and simulated subhalo catalogues used are available at <https://www.ict.inaf.it/index.php/DOI/122-ds-2020-1>.

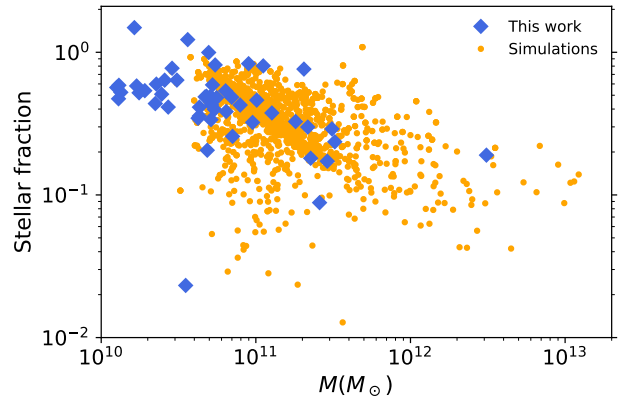


Fig. 10. Comparison between the values of the stellar over total mass fraction of sub-haloes with velocity dispersion greater than 80 km s^{-1} as a function of their total mass. In blue: values predicted by our model. In orange: values predicted by hydrodynamical simulations.

of massive galaxy clusters, including the model of AS1063 by B19, and a set of 25 clusters of similar mass and redshift from the cosmological simulations presented in [Planelles et al. \(2014\)](#) and [Rasia et al. \(2015\)](#), which incorporate gas cooling, star formation, and energy feedback from supernovae and accreting SMBHs. They found that the probability of producing galaxy-scale strong lensing events is for observed clusters around an order of magnitude bigger than it is for simulated clusters. To interpret this discrepancy, they considered the relation between the mass of the sub-haloes in the model and their maximum circular velocity, defined as $v_{max} = \max \sqrt{\frac{GM}{r}}$ (for an isothermal model, $v_{max} = \sqrt{2}\sigma_0$). M20 found that, at fixed total sub-halo mass, the value of the maximum circular velocity of cluster substructures is larger than what cosmological simulations predict. This seems to indicate that simulated cluster members are, on average, less compact than observed.

Some other recent results, using the higher-resolution simulations from the Hydrangea/C-EAGLE suite ([Bahé et al. 2017](#); [Barnes et al. 2017](#)), do not claim the same large discrepancy in terms of galaxy scale lensing events and of sub-halo compactness ([Robertson 2021](#); [Bahé 2021](#), hereafter B21). Studying simulated clusters, B21 reported a bi-modal $v_{max}(M)$ function, with a lower sequence of sub-haloes with a baryon fraction smaller than 0.1 dominating for $M < 10^{11} M_{\odot}$, and a second sequence for higher sub-halo mass values. This last branch yields results consistent with those of the lensing models presented in M20.

All SL models included in M20 used two optimised power-law scaling relations to model the truncation radius and the velocity dispersion of the cluster members from their luminosity. As all cluster models represent sub-haloes with isothermal profiles, this also leads to a fixed power-law relation between the maximum circular velocity (which is proportional to the velocity dispersion) of each sub-halo and its mass. On the other hand, our new method to assign mass to sub-haloes again avoids a fixed power law between the two quantities, allowing for the inclusion of some scatter. In Fig 11, we show the $v_{max}(M)$ relation obtained from our model for all the members with $M > 10^{10} M_{\odot}$ compared with that from B19: the two models agree well in the entire mass range considered.

Comparing our results with those shown in Figure 3 from B21, we notice that our relation matches fairly well with the

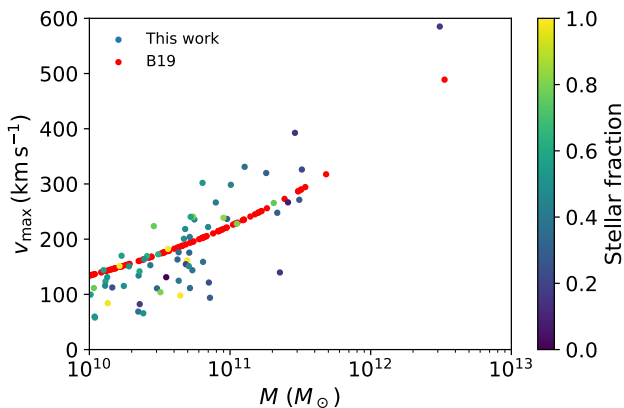


Fig. 11. Maximum circular velocity of the cluster members as a function of their total mass. In red: values predicted by the model presented in B19. Our values are color-coded according to the predicted stellar over total mass fraction. Only members with $M > 10^{10} M_{\odot}$ are shown.

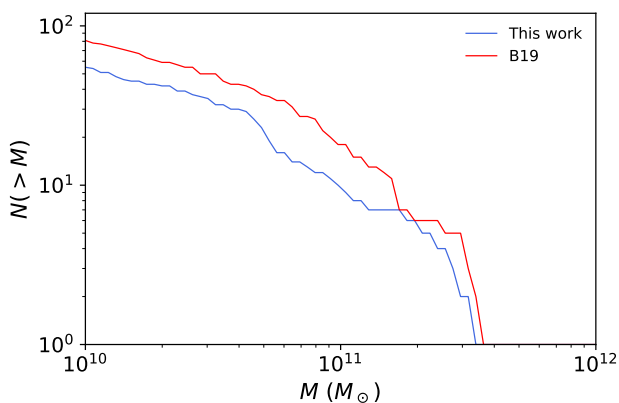


Fig. 12. Cumulative sub-halo mass function for the members within a projected radius of $0.15r_{\text{vir}}$ predicted by our model (in blue) by that presented in B19 (in red).

higher-mass branch of the Hydrangea hydrodynamic simulations, both in terms of circular velocity and of the stellar fraction of the cluster members at a fixed total mass. However, we note that the high-mass branch that agrees with our model in terms of maximum circular velocity is not found, for instance, in the Illustris-TNG300s simulation (Marinacci et al. 2018; Naiman et al. 2018; Nelson et al. 2018; Pillepich et al. 2018; Springel et al. 2018), which have a comparable resolution, as shown in Figure 4 from B21. Furthermore, Ragone-Figueroa et al. (2018) also found that the Hydrangea simulations produce galaxies with a very high total mass which may not agree with observations. On the other hand, as already visible from Fig 11, we do not find the large number of sub-haloes with $M < 10^{11} M_{\odot}$, $v_{\text{max}} < 100 \text{ km s}^{-1}$, and a low stellar fraction predicted by the lower sequence by B21. As a consequence, our model predicts, on average, higher maximum circular velocities with respect to simulations for sub-haloes with mass between 10^{10} and $10^{11} M_{\odot}$. In this total mass range, we find just a few members with maximum circular velocity lower than 100 km s^{-1} , while in B21 most of the galaxies lie below this threshold. This seems to confirm the discrepancy reported by M20 in terms of galaxy-scale SL events, as most of these events are caused by haloes in this mass

range, at least for AS1063 and the other clusters with a similar mass. We finally note that in B21 the values of the baryon fractions are computed within a radius of 30 kpc, while in our work they are the ratio between the total stellar mass the total mass of each sub-halo. However, nearly all members in our model have a truncation radius smaller than 30 kpc, which allows us to safely compare the two estimates.

The comparative lack of low-mass members in our model is reflected by the cumulative sub-halo mass function within a projected radius of $0.15r_{\text{vir}}$, shown in Figure 12: our model agrees with the results presented in B19, which in turn found a lower cumulative mass function compared to that of the simulations, particularly considering sub-haloes with $M < 10^{11} M_{\odot}$ and $v_{\text{max}} < 100 \text{ km s}^{-1}$, as reported by B21 in Figure 1. In the same mass range, our cumulative sub-halo mass function has a slope similar to that by B19, significantly shallower than that from the cosmological simulations presented in B21. In the radial range considered, our sample of photometric cluster members is highly complete down to $m_{\text{F160W}} = 24$.

8. Conclusions

In this article, we have presented an improved SL model of the Hubble Frontier Fields galaxy cluster AS1063, thanks to new measurements of the structural parameters, namely magnitude, effective radius, and Sérsic index, of the cluster members. We have also exploited the values of the central stellar velocity dispersion of several luminous members, obtained from MUSE integral-field spectroscopy, to calibrate the FP relation for the cluster.

We use the FP to estimate the value of the central velocity dispersion of each cluster member from its observed magnitude and effective radius and we choose to consider a proportionality relation between the values of the effective R_e and truncation r_t radii. This allows us to assign a value of total mass to every cluster member, which does not depend only on the total luminosity of a galaxy. The main results and conclusions of our analysis are here summarised:

1. We find that the lowest value of the rms difference between the observed and model-predicted positions of the 55 considered multiple images (from 20 background sources) is obtained when $r_t = 2.3R_e$ for all cluster members.
2. Our method allows us to determine a relation between the total mass and velocity dispersion of the cluster members which is more realistic than the simple power law used in B19. Specifically, the new relation has some visible scatter and is less steep than that recently found in B19.
3. A more accurate estimate of the total mass of the cluster members allows for a reduction of the scatter on the determination of some parameters of the diffuse component. In particular, the statistical uncertainty on the value of the core radius of the main DM halo decreases by more than 30% compared to previous studies.
4. We confirm that modelling the main DM haloes of massive galaxy clusters with isothermal mass density profiles requires the presence of significantly large core radii. The value of the core radius of the main DM halo of AS1063 is $86 \pm 2 \text{ kpc}$.
5. From our model and from the sampling of the posterior probability distribution of the parameters, we obtain the cumulative projected mass profiles of the various cluster components. Thanks to Chandra X-ray observations and to the new measurements of the cluster members stellar mass values,

we can disentangle the hot gas and stellar mass profiles. At a distance from the cluster centre of 350 kpc, the cumulative, projected stellar, hot-gas, and baryonic fractions are, respectively, 0.6%, 14.1%, and 14.7%, the latter close to the cosmological value found by [Planck Collaboration et al. \(2020\)](#).

6. For the high-mass members included in our model, the median value of the stellar over total mass fraction is 0.48, with a standard deviation of 0.26. Considering, instead, the ratio between the stellar and total mass, both predicted within the effective radius, we find very good agreement with the relation obtained by [Grillo \(2010\)](#) on a wide sample of SDSS early-type galaxies.
7. We use the stellar-to-halo mass relation from [Girelli et al. \(2020\)](#), based on the Λ CDM DUSTGRAIN-*pathfinder* *N*-body simulation, to obtain the halo mass value of our cluster members from their measured stellar mass value. We find that the SHMR predicts a median value of the stellar fraction of the high-mass cluster members smaller by almost an order of magnitude with respect to our model.
8. We compare the high-mass cluster members with a catalogue of simulated sub-haloes. We extract the substructures from the projected cores of 18 clusters from recent cosmological hydrodynamical simulations ([Planelles et al. 2014](#); [Rasia et al. 2015](#)), imposing the same selection criterion on their velocity dispersion. We report good agreement between the values of the stellar over total fractions of the two samples.
9. We study the relation between maximum circular velocity and total mass of the sub-haloes, which is an indication of their compactness. We find a good agreement with what reported by B19. Comparing our results with those obtained by B21 from the simulated clusters of the Hydrangea/C EAGLE suite, we obtain consistent results for sub-halos with total mass greater than $10^{11} M_{\odot}$. On the contrary, we do not observe the large number of sub-haloes with mass below $10^{11} M_{\odot}$ and low baryon fraction predicted by B21. In this sub-halo mass range our relation predicts, on average, higher v_{\max} at a fixed total mass, in agreement with the predictions of B19 and M20. This corresponds to haloes that are more compact than those in the hydrodynamical simulations. As a consequence, in the same total mass range our cumulative sub-halo mass function has a shallower slope compared to what reported by B21, very similar to that by B19 and M20.

Similar analyses may be performed on other massive clusters, for which MUSE data are available, to test the robustness of the results obtained with the new methodology presented here.

Acknowledgements. We acknowledge financial support by PRIN-MIUR 2017WSCC32 "Zooming into dark matter and proto-galaxies with massive lensing clusters" (P.I.: P. Rosati), INAF "main-stream" 1.05.01.86.20 (P.I.: M. Nonino) and INAF 1.05.01.86.31 (P.I.: E. Vanzella). GG thanks Ana Acebron Muñoz and Andrea Bolamperti for their help and suggestions. PB acknowledges financial support from ASI through the agreement ASI-INAF n. 2018-29-HH.0. MM acknowledges support from ASI through the grants ASI-INAF n. 2018-23-HH.0 and ASI-INAF n.2017-14-H.0. GBC acknowledges the Max Planck Society for financial support through the Max Planck Research Group for S. H. Suyu and the academic support from the German Centre for Cosmological Lensing.

References

Abell, G. O., Corwin, Harold G., J., & Olowin, R. P. 1989, *ApJS*, 70, 1
 Agnello, A., Evans, N. W., & Romanowsky, A. J. 2014, *MNRAS*, 442, 3284
 Annunziatella, M., Bonamigo, M., Grillo, C., et al. 2017, *ApJ*, 851, 81
 Bacon, R., Accardo, M., Adjali, L., et al. 2010, in *Society of Photo-Optical Instrumentation Engineers (SPIE) Conference Series*, Vol. 7735, *Ground-based and Airborne Instrumentation for Astronomy III*, ed. I. S. McLean, S. K. Ramsay, & H. Takami, 773508

Bahé, Y. M. 2021, *MNRAS*[arXiv:2101.12112]
 Bahé, Y. M., Barnes, D. J., Dalla Vecchia, C., et al. 2017, *MNRAS*, 470, 4186
 Barnes, D. J., Kay, S. T., Bahé, Y. M., et al. 2017, *MNRAS*, 471, 1088
 Barr, J., Jørgensen, I., Chiboucas, K., Davies, R., & Bergmann, M. 2006, *ApJ*, 649, L1
 Bender, R., Burstein, D., & Faber, S. M. 1992, *ApJ*, 399, 462
 Bergamini, P., Rosati, P., Mercurio, A., et al. 2019, *A&A*, 631, A130
 Bertin, E. & Arnouts, S. 1996, *A&AS*, 117, 393
 Bonamigo, M., Grillo, C., Ettori, S., et al. 2018, *ApJ*, 864, 98
 Calzetti, D., Armus, L., Bohlin, R. C., et al. 2000, *ApJ*, 533, 682
 Caminha, G. B., Grillo, C., Rosati, P., et al. 2016, *A&A*, 587, A80
 Caminha, G. B., Rosati, P., Grillo, C., et al. 2019, *A&A*, 632, A36
 Cappellari, M. & Emsellem, E. 2004, *PASP*, 116, 138
 Cappellari, M., Scott, N., Alatalo, K., et al. 2013, *MNRAS*, 432, 1709
 Chabrier, G. 2003, *PASP*, 115, 763
 Coe, D., Salmon, B., Bradač, M., et al. 2019, *ApJ*, 884, 85
 De Grandi, S., Böhringer, H., Guzzo, L., et al. 1999, *ApJ*, 514, 148
 De Lucia, G., Kauffmann, G., Springel, V., et al. 2004, *MNRAS*, 348, 333
 Diego, J. M., Molnar, S. M., Cerny, C., et al. 2020, *ApJ*, 904, 106
 Diemand, J. & Moore, B. 2011, *Advanced Science Letters*, 4, 297
 Djorgovski, S. & Davis, M. 1987, *ApJ*, 313, 59
 Dolag, K., Borgani, S., Murante, G., & Springel, V. 2009, *MNRAS*, 399, 497
 Dressler, A., Lynden-Bell, D., Burstein, D., et al. 1987, *ApJ*, 313, 42
 Einasto, J. 1965, *Trudy Astrofizicheskogo Instituta Alma-Ata*, 5, 87
 Elíasdóttir, A., Limousin, M., Richard, J., et al. 2007, arXiv e-prints, arXiv:0710.5636
 Faber, S. M. & Jackson, R. E. 1976, *ApJ*, 204, 668
 Ghosh, A., Williams, L. L. R., & Liesenborgs, J. 2021, *MNRAS*[arXiv:2104.11781]
 Giocoli, C., Baldi, M., & Moscardini, L. 2018, *MNRAS*, 481, 2813
 Girelli, G., Pozzetti, L., Bolzonella, M., et al. 2020, *A&A*, 634, A135
 Gómez, P. L., Valkonen, L. E., Romer, A. K., et al. 2012, *AJ*, 144, 79
 Grillo, C. 2010, *ApJ*, 722, 779
 Grillo, C., Suyu, S. H., Rosati, P., et al. 2015, *ApJ*, 800, 38
 Jullo, E. & Kneib, J. P. 2009, *MNRAS*, 395, 1319
 Jullo, E., Kneib, J. P., Limousin, M., et al. 2007, *New Journal of Physics*, 9, 447
 Karman, W., Caputi, K. I., Caminha, G. B., et al. 2017, *A&A*, 599, A28
 Karman, W., Caputi, K. I., Grillo, C., et al. 2015, *A&A*, 574, A11
 Kneib, J. P., Ellis, R. S., Smail, I., Couch, W. J., & Sharples, R. M. 1996, *ApJ*, 471, 643
 Koopmans, L. V. E., Bolton, A., Treu, T., et al. 2009, *ApJ*, 703, L51
 Koopmans, L. V. E., Treu, T., Bolton, A. S., Burles, S., & Moustakas, L. A. 2006, *ApJ*, 649, 599
 Kravtsov, A. V. 2013, *ApJ*, 764, L31
 Lagattuta, D. J., Richard, J., Clément, B., et al. 2017, *MNRAS*, 469, 3946
 Limousin, M., Kneib, J.-P., & Natarajan, P. 2005, *MNRAS*, 356, 309
 Limousin, M., Richard, J., Jullo, E., et al. 2016, *A&A*, 588, A99
 Lotz, J. M., Koekemoer, A., Coe, D., et al. 2017, *ApJ*, 837, 97
 Marinacci, F., Vogelsberger, M., Pakmor, R., et al. 2018, *MNRAS*, 480, 5113
 Meneghetti, M., Davoli, G., Bergamini, P., et al. 2020, *Science*, 369, 1347
 Meneghetti, M., Natarajan, P., Coe, D., et al. 2017, *MNRAS*, 472, 3177
 Mo, H. J., Mao, S., & White, S. D. M. 1998, *MNRAS*, 295, 319
 Monna, A., Seitz, S., Balestra, I., et al. 2017, *MNRAS*, 466, 4094
 Monna, A., Seitz, S., Zitrin, A., et al. 2015, *MNRAS*, 447, 1224
 Moore, B., Ghigna, S., Governato, F., et al. 1999, *ApJ*, 524, L19
 Moster, B. P., Somerville, R. S., Maibetsch, C., et al. 2010, *ApJ*, 710, 903
 Munari, E., Grillo, C., De Lucia, G., et al. 2016, *ApJ*, 827, L5
 Naiman, J. P., Pillepich, A., Springel, V., et al. 2018, *MNRAS*, 477, 1206
 Natarajan, P. & Kneib, J.-P. 1997, *MNRAS*, 287, 833
 Navarro, J. F., Frenk, C. S., & White, S. D. M. 1996, *ApJ*, 462, 563
 Navarro, J. F., Frenk, C. S., & White, S. D. M. 1997, *ApJ*, 490, 493
 Nelson, D., Pillepich, A., Springel, V., et al. 2018, *MNRAS*, 475, 624
 Peng, C. Y., Ho, L. C., Impey, C. D., & Rix, H.-W. 2010, *AJ*, 139, 2097
 Pillepich, A., Nelson, D., Hernquist, L., et al. 2018, *MNRAS*, 475, 648
 Planck Collaboration, Aghanim, N., Akrami, Y., et al. 2020, *A&A*, 641, A6
 Planelles, S., Borgani, S., Fabjan, D., et al. 2014, *MNRAS*, 438, 195
 Postman, M., Coe, D., Benítez, N., et al. 2012, *ApJS*, 199, 25
 Ragone-Figueroa, C., Granato, G. L., Ferraro, M. E., et al. 2018, *MNRAS*, 479, 1125
 Rahaman, M., Raja, R., Datta, A., et al. 2021, *MNRAS*, 505, 480
 Raney, C. A., Keeton, C. R., Brennan, S., & Fan, H. 2020, *MNRAS*, 494, 4771
 Rasia, E., Borgani, S., Murante, G., et al. 2015, *ApJ*, 813, L17
 Remolina González, J. D., Sharon, K., & Mahler, G. 2018, *ApJ*, 863, 60
 Richard, J., Jauzac, M., Limousin, M., et al. 2014, *MNRAS*, 444, 268
 Robertson, A. 2021, *MNRAS*, 504, L7
 Rosati, P., Balestra, I., Grillo, C., et al. 2014, *The Messenger*, 158, 48
 Salpeter, E. E. 1955, *ApJ*, 121, 161
 Sand, D. J., Treu, T., Smith, G. P., & Ellis, R. S. 2004, *ApJ*, 604, 88
 Sartoris, B., Biviano, A., Rosati, P., et al. 2020, *A&A*, 637, A34
 Scoville, N., Aussel, H., Brusa, M., et al. 2007, *ApJS*, 172, 1
 Smith, R., Choi, H., Lee, J., et al. 2016, *ApJ*, 833, 109
 Speagle, J. S., Steinhardt, C. L., Capak, P. L., & Silverman, J. D. 2014, *ApJS*, 214, 15
 Springel, V. 2005, *MNRAS*, 364, 1105
 Springel, V., Pakmor, R., Pillepich, A., et al. 2018, *MNRAS*, 475, 676
 Springel, V., White, S. D. M., Tormen, G., & Kauffmann, G. 2001, *MNRAS*, 328, 726
 Tormen, G. 1997, *MNRAS*, 290, 411
 Tortorelli, L., Mercurio, A., Paolillo, M., et al. 2018, *MNRAS*, 477, 648
 Umetsu, K., Zitrin, A., Gruen, D., et al. 2016, *ApJ*, 821, 116
 Vazdekis, A., Sánchez-Blázquez, P., Falcón-Barroso, J., et al. 2010, *MNRAS*, 404, 1639
 Wang, J., Bose, S., Frenk, C. S., et al. 2020, *Nature*, 585, 39